Research Square

Preprints are preliminary reports that have not undergone peer review.
They should not be considered conclusive, used to inform clinical practice,
or referenced by the media as validated information.

Tracking Transcrustal Magma Ascent Beneath Laguna del Maule, Chile

Jim Bradford

JimBradford@arizona.edu

University of Arizona https://orcid.org/0000-0003-1391-4779

Sankha Subhra Mahanti

University of Arizona

Eric Kiser

University of Arizona

Susan Beck

University of Arizona

Martin Fernandez

Universidad Nacional de San Juan

Sol Trad

Universidad Nacional de San Juan

Ryan Porter

Northern Arizona University https://orcid.org/0000-0001-6353-9191

Sebastian Tauber

Northern Arizona University

Ariane Maharaj

University of Lausanne

Hannah Howe

University of Alberta

Gustavo Federico Ortiz

Universidad Nacional de San Juan

Mauro Saez

Consejo Nacional de Investigaciones Científicas y Técnicas (CONICET), Universidad Nacional de San Juan

Article

Keywords:

Posted Date: November 28th, 2025

DOI: https://doi.org/10.21203/rs.3.rs-8060109/v1

License: This work is licensed under a Creative Commons Attribution 4.0 International License.
Read Full License

Additional Declarations: There is **NO** Competing Interest.

Tracking Transcrustal Magma Ascent Beneath Laguna del Maule, Chile

Authors:

Jim Bradford (1), Sankha Subhra Mahanti (1), Eric Kiser (1), Susan Beck (1),

Martin Fernandez (2), Sol Trad (3,4),

Ryan Porter (5), Sebastian Tauber (5),

Ariane Maharaj (6), Hannah Howe (7),

Gustavo Federico Ortiz (2), Mauro Saez (2,4)

Affiliations:

(1) Department of Geosciences, University of Arizona

(2) Departamento de Geofísica y Astronomía, Universidad Nacional de San Juan

(3) Center for Research on the Geosphere and Biosphere (CIGEOBIO), Universidad Nacional de San Juan

(4) Consejo Nacional de Investigaciones Científicas y Técnicas (CONICET), Universidad Nacional de San Juan

(5) School of Earth Sciences and Environmental Sustainability, Northern Arizona University

(6) Institute of Earth Sciences, University of Lausanne

(7) Department of Physics, University of Alberta

0.0 Abstract

There is abundant evidence that arc volcanoes are fed by complex networks of storage zones that extend throughout the crust. Though the geometric details of these transcrustal magmatic systems are well resolved beneath several volcanic settings, the relationship between magma transport at depth and volcanic unrest at the surface remains poorly constrained. At Laguna del Maule in central Chile, the site of several Holocene silicic eruptions and present-day surface uplift, we show that seismically imaged magma reservoirs in the upper and lower crust are connected by a zone of deep crustal seismicity. A pronounced one-day swarm of this seismicity in 2018 was followed 3 months later by an increase in the inflation rate observed at the surface. We infer that this earthquake swarm was driven by the injection of a new batch of melt, transported between lower to upper crust magma reservoirs. The lag time between melt transport and surface inflation was governed by the hydraulic diffusivity of the upper crustal reservoir. These results indicate that volcanic unrest at Laguna del Maule begins deep within the crust and

months before observable signals of shallow magma reservoir pressurization and may be replicable for volcanic arcs worldwide.

1.0 Introduction

Over 500 million people are at risk from volcanic hazards, the majority of whom live near volcanic arcs formed due to the subduction of oceanic lithosphere (Doocy et al., 2013). Within the subduction system, arc magmas are generated by hydrating the mantle wedge with fluids supplied by the subducting plate. These magmas buoyantly rise and are emplaced within the overriding crust where they may stall and evolve through processes of crystal fractionation and assimilation of the continental crust (e.g., Hildreth & Moorbath, 1988; Ulmer, 2001; Grove et al., 2012). Despite the central role magma evolution plays within arc volcanism and the formation of evolved continental crust, how magma is stored and develops within the mantle wedge and lower continental crust is poorly constrained. Furthermore, we know little about the deep and transcrustal processes involved in eruptions and about the interplay between crustal structures, magma movement, associated seismicity, and how these may be precursory to eruptions.

Ascending magma is commonly associated with volcano-tectonic earthquakes occurring at crustal depths (e.g., Chouet, 1996; Konstantinou, 2024). These events are often interpreted as signals of magma rising through crustal plumbing systems to recharge upper crust magma chambers through dike intrusions, which may produce surface deformation and uplift (e.g., Cesca et al., 2020). The Laguna Del Maule (LdM) volcanic complex of Chile and Argentina (Figure 1) is one such example where surficial deformation is being closely monitored. The LdM volcanic complex (~36ºS, ~75ºW) is an active silicic system in the south-central Andes that has experienced several caldera-forming eruptions within the last 23,000 years and has deposited more than 350 km^3 of volcanic material within the last 1.5 Ma (Hildreth and Fierstein, 2024). The complex is composed of several monogenetic and polygenetic vents of erupted basalt through rhyolite compositions, as well as several caldera forming ignimbrite deposits (Drake, 1976; Hildreth et al., 2009; Hildreth & Fierstein, 2024). Since 2007, LdM has exhibited significant unrest, with rapid surficial uplift rates exceeding 20 cm/yr and signs of magma intruding into shallow storage levels (Feigl et al., 2014; Le Mével et al., 2015; Le Mével et al., 2021). Erupted rhyolitic melt inclusions indicate that magmas have ascended from ~14 to 4 km depth (Klug et al., 2020), estimates that are corroborated by geophysical evidence for shallow crustal storage within the upper 15 km (Cáceres Acevedo, 2016; Cáceres et al., 2018; Cordell et al., 2018; Wespestad et al., 2019; Bai et al., 2020; Rojas et al., 2022). To incubate and resupply this system with accessory minerals, a lower crust magma storage must be present, implicating a vertically extensive, transcrustal magmatic plumbing network (Annen et al., 2005; Cashman et al., 2017). LdM presents an opportunity to investigate these

transcrustal processes and melt migration within a cordilleran-arc setting, which may be applied to subduction-related volcanic arcs worldwide. With this, we may deepen our understanding of the relationship between magma movement, surficial deformation, and global volcanic hazards.

To investigate these problems, we utilize the spatially dense seismometer arrays from the Trans-Andean Great Orogeny (TANGO; Beck et al., 2022a, 2022b) and Laguna Del Maule seismic imaging (LaMa; Thurber, 2015) deployments to constrain seismicity and crustal structure beneath LdM (Figure 1). In this study, we present our findings at LdM as an outstanding example of an active volcanic system where we have captured transcrustal processes by combining earthquake locations and seismic imaging to constrain the migration of melt between storage zones through the lower and upper crust.



Figure 1. Topographic map of the Andean Cordillera centered at the Laguna Del Maule volcanic complex showing the Holocene and Pleistocene volcanoes (Global Volcanism Program, 2025), seismic stations, and GPS station MAU2 along with cross section profile lines. Line *ABC* approximately follows the trend of the TANGO

nodal network line. The blue box in the inset map shows the study area within the Andean Southern Volcanic Zone.

2.0 LdM Seismicity

3860 well-constrained events are detected between 2015-2018 using the data from the LaMa network and 499 events are obtained in 2022-2024 using the TANGO data. Most of the events found within the TANGO dataset were recorded between January-May 2023 as the nodal array was active only for those months. Since the nodal array is located to the north of LDM volcanic field, significantly fewer well-constrained events are obtained with the TANGO dataset as compared to the LaMa network due to poor azimuthal coverage. Overall, the location uncertainties of these events are also higher than the 2015-2018 events due to this station coverage difference.

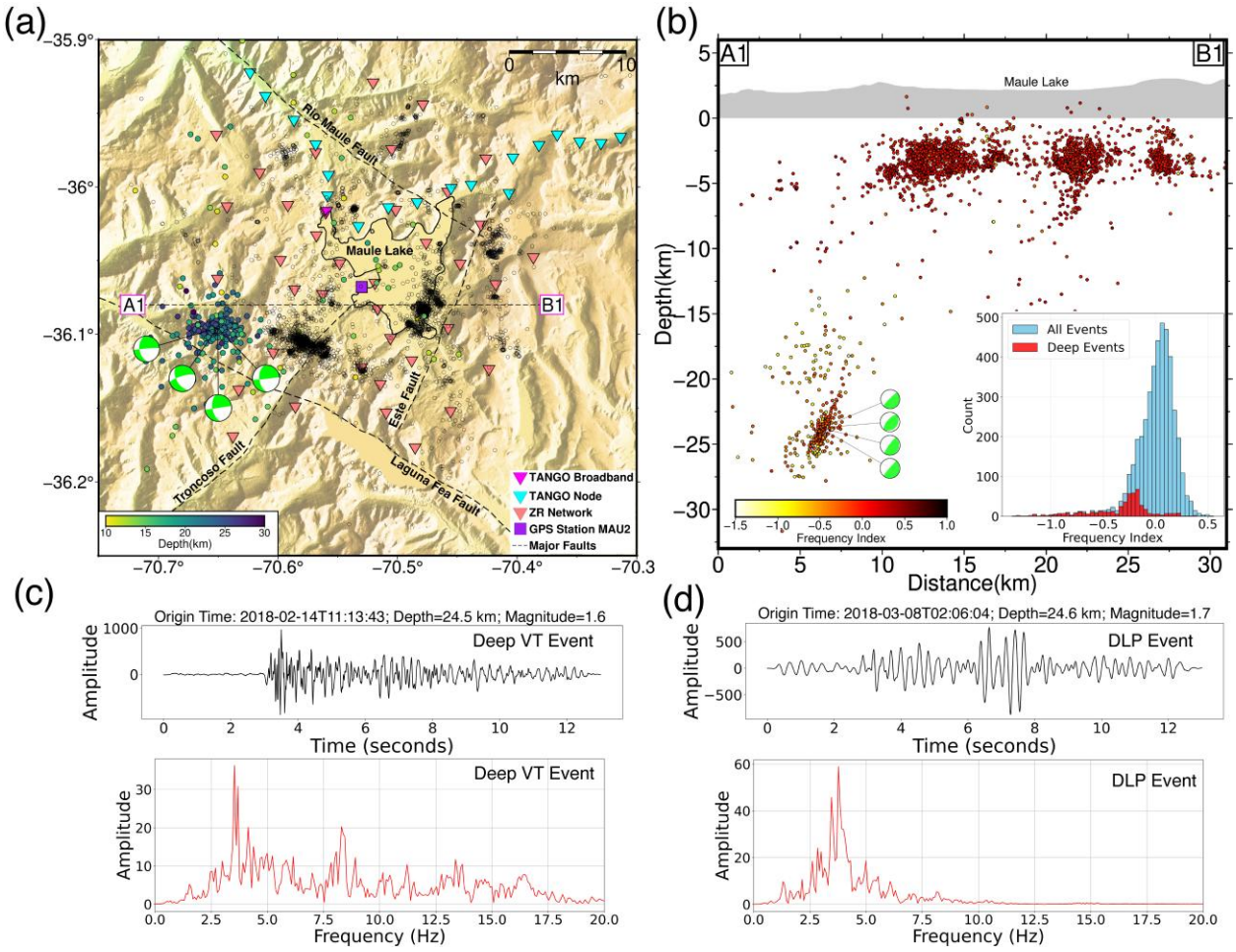


Figure 2. (a) Seismicity constrained in this study plotted on the map as circles color coded by depth for events >10 km depth. Shallow events at <10 km depth are plotted as open circles to highlight the deeper events plotted as solid circles. Focal

mechanisms of four volcano-tectonic (VT) swarm events are shown as well. Major crustal faults are marked and labeled. (b) Seismicity and focal mechanisms are projected along cross-section line A-B marked in (a) and events are color coded by frequency index. The histogram in the inset shows the distribution of frequency index of all events (blue) and events deeper than 10 km (red). Example trace and frequency spectrum at station W2P of the LaMa network for (c) a deep VT event and (d) a DLP event of similar magnitude and depth.

The combined event distribution map (Figure 2) shows two large clusters of shallow seismicity to the southwest and eastern edge of the Maule Lake along with several small clusters to the north of the lake. This spatial distribution of seismicity surrounding the Maule Lake in general matches with previous studies (Cardona et al., 2018; Peterson et al., 2020; Vigide et al., 2025). However, significantly more events are observed in 2015-2018 as recorded by the LaMa network data compared to these previous studies. These shallow events have been associated with deformation along the fault systems surrounding the Maule Lake potentially triggered by magma intrusions (e.g. Cardona et al., 2018). In addition to this shallow seismicity, a significant number of events are observed at ~12-30 km depth west of Maule Lake along with a cluster of events at ~21-26 km depth. The frequency index analysis (Buurman & West, 2010; Wilding et al., 2023) suggests a mixture of high and low frequency content for these deeper earthquakes. The cluster of events at ~21-26 km depth is vertically extended and consists of events with similar magnitude and high frequency index (Figure 2b), all of which occurred on a single day (February 14, 2018). We interpret these as a mid-crustal volcano-tectonic (VT) swarm beneath the LDM volcanic field (Figure 2, Supplementary Figure S5). The rest of the deep seismicity mostly exhibits low-frequency index, and we identify these earthquakes as deep long-period (DLP) events. To our best knowledge, this is the first study to find well-constrained DLP events in the Andes, though this form of seismicity has been identified at several volcanic regions around the world (e.g. White et al., 1996; Nichols et al., 2011; Wech et al., 2020; Song et al., 2023).

3.0 LdM Crustal Structure

To constrain crustal structure beneath LdM, we calculate P-Receiver Functions (RFs) to estimate the depths to strong discontinuities within the subsurface (Langston, 1979). RFs are time-domain waveforms containing a distribution of positive and negative amplitudes that, to first order, signal the broad transitions in seismic impedance occurring over a few kilometers or less within the crust and upper mantle (Rychert et al., 2007; Rondenay, 2009). RF pulse width and amplitude approximately correspond respectively to the length and magnitude of velocity

changes along the ray path (Cassidy, 1992; Rychert et al., 2007; Levin et al., 2016). Within our depth-migrated image, successive negative-positive amplitudes with depth indicate the presence of crustal low-velocity zones (LVZs) with their pulses, respectively, marking the tops and bases of the LVZs. We examine high-frequency RFs (~3.7 Hz), which can coherently resolve layers over a range of 1-2 km thickness (Cassidy, 1992).

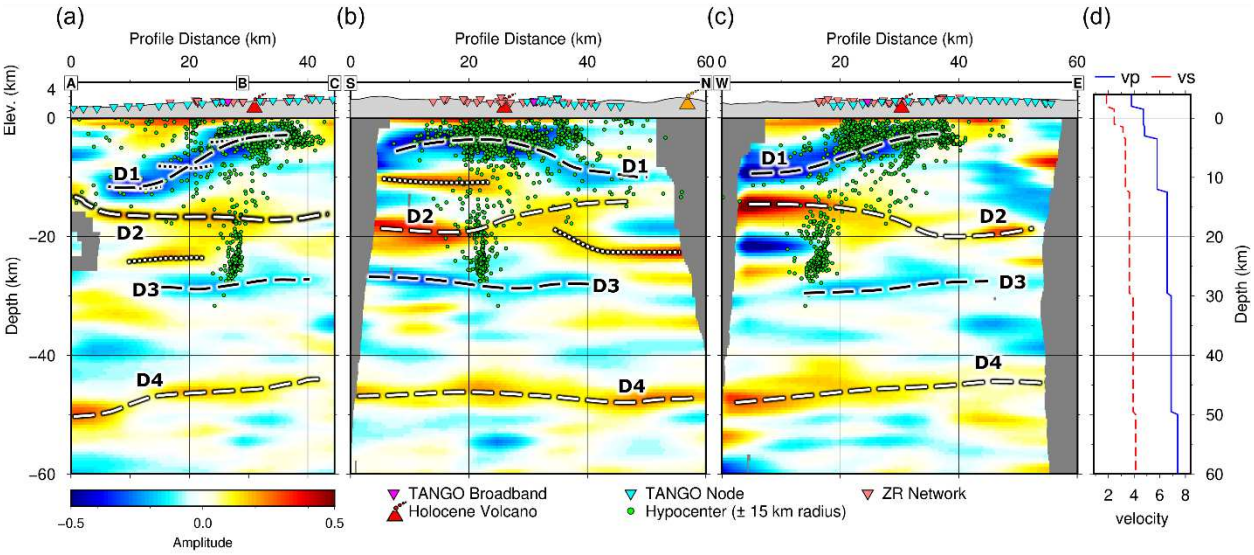


Figure 3. Common Conversion Point (CCP) stack using 3.7 Hz Receiver Functions (RFs). (a) Slice through CCP volume along line *ABC*, note that point B is a kink in the line, (b) south-north slice centered at point *B*, (c) west-east slice centered at point *B*, (d) modified output VELEST model from hypocenter locations. Major (dashed) and minor (dotted) discontinuities in amplitude and size are outlined and labeled in the downward order they appear. In the CCP migration, stacking bins that contained less than 20 piercing points within the 12 km range or less than 2 piercing points within the 4 km standard deviation weighting range were colored gray. All depths are below sea level *(bsl*). Seismicity within 15 km of each line are orthogonally projected onto the cross-section panels.

We identify several major crustal discontinuities but focus here on four that lie directly below the LdM edifice and encompass the detected seismicity. Labeled in order of increasing depth from D1-D4 (Figure 3a,b,c), these discontinuities respectively mark strong downward velocity changes interpreted as: (1) a shallow low velocity zone (LVZ) bounded at the top by negative discontinuity D1 (~12 to ~3 km *bsl)* indicating velocity decrease and at its base by a positive discontinuity D2 (~16 km *bsl)* indicating a velocity increase, (2) a lower crustal LVZ with negative discontinuity D3 (~28 km bsl) marking its top and without an apparent base, and (3) the continental Moho marked as positive discontinuity D4 (~46 km *bsl)*.

We interpret the upper crustal LVZ as the primary upper crust storage zone for LdM silicic volcanism. The southward extent of D1 and D2 continues past the range of seismic stations where we lose resolvability. The LVZ is generally northwest dipping and agrees well in depth and trend from prior interpretations (Wespestad et al., 2019), but is larger than other estimates of the LdM magma chamber size (Miller et al., 2017; Cordell et al., 2018; Wespestad et al., 2019; Bai et al., 2020). However, our results do encompass all currently existing estimates together. The sensitivity of RFs to velocity and density changes within the scope of the upper 5 km around Maule Lake may measure a generalized zone of negative impedance change due to a combination of hydrothermal and partial melt volumes.

We observe clustered shallow seismicity along much of the D1 discontinuity, likely related to stress perturbations from the inferred shallow magma reservoir. Below D1 and above D2 seismicity becomes diffuse, but is largely bounded by these interfaces. Below D2, seismicity is localized in the form of the deep cluster of VT and DLP events which extends to the D3 interface. The negative amplitudes of D3 and other nearby discontinuities indicate some degree of partial melt is present to reduce the velocities of what may be presumed to be granulitic and mafic lower crust (Rudnick & Fountain, 1995; Hacker et al., 2015). Melt within this region of the crust may contain a lower fraction of silica and be heterogeneously distributed through progressively amalgamated sill complexes (Glazner et al., 2004; Jaxybulatov et al., 2014; Huang et al., 2015). The LVZ between D3 and the continental Moho may be a large complex hosting crustal assimilation and fractional crystallization like in the models for a MASH complex or Deep Hot Crustal Zone (Hildreth & Moorbath, 1988; Annen et al., 2005). The relatively thick crust provides a large zone in the lower 20 km for melts to chemically evolve and segregate, allowing more buoyant magmas to rise toward the upper crust for additional staging (Annen et al., 2005; Dufek & Bergantz, 2005; Farner & Lee, 2017).

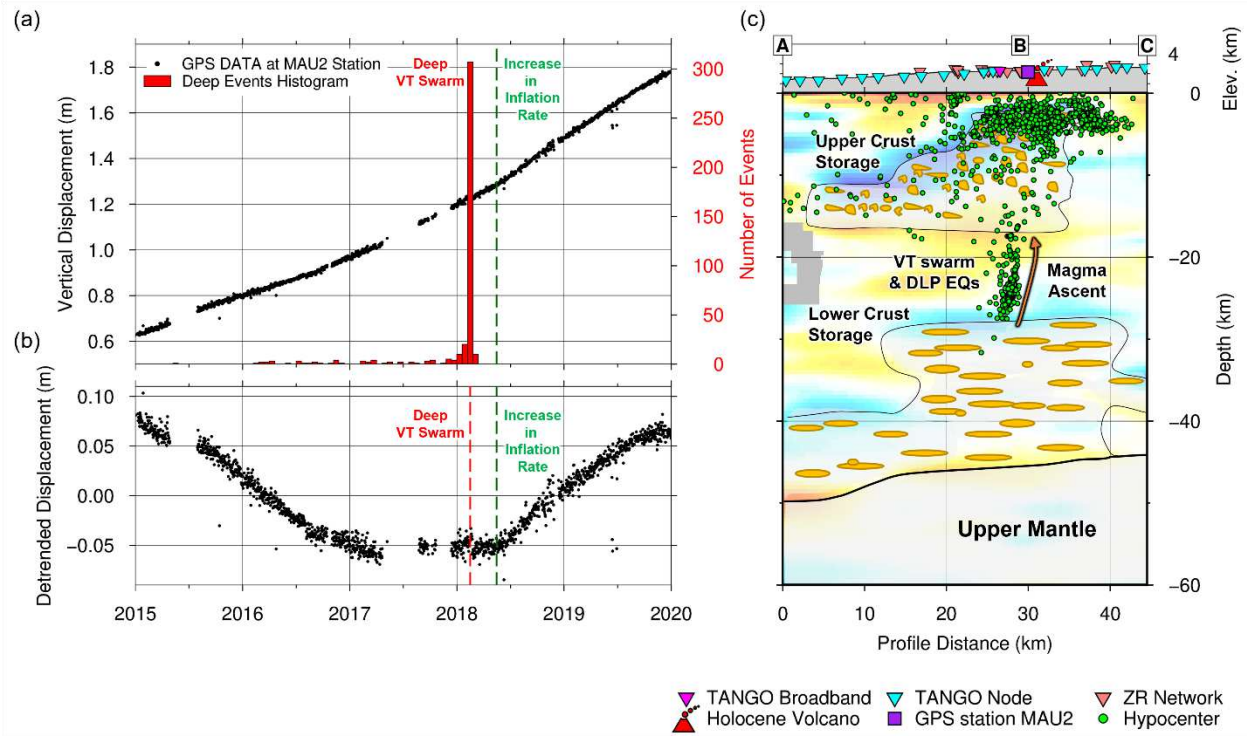


Figure 4. (a) Vertical displacement data from GPS station MAU2, located at the southwestern edge of Maule Lake (Le Mével et al., 2021) plotted alongside the event frequency histogram of events at depth>10 km highlighting the deep VT swarm. (b) The same GPS data after the linear trend is removed for data between 2015 and 2020. The VT swarm is marked with the red dashed line. An acceleration of surface uplift, marked by the green dash line, occurs ~3 months after the swarm (c) Schematic interpretation of the Laguna Del Maule crust from seismicity and receiver function results in this study. An episode of magma ascending between lower and upper crustal storage zones is marked by deep seismicity between the two reservoirs.

4.0 A Transcrustal Signal of Volcanic Unrest

The comparisons above show that the characteristics of seismicity change across the interfaces that define the top and bottom boundaries of inferred magma reservoirs in the upper and lower crust. The seismicity that occurs between the upper and lower reservoirs is perhaps the most intriguing both because of its unusual depths and its intense spatiotemporal clustering. Given the context of the imaged magmatic system geometry, we interpret both the DLP and VT events in the region as direct evidence of magma transport from the lower crustal magma storage zone into the upper crustal magma reservoir through dike-like conduits. Furthermore, the VT swarm on February 14, 2018, indicates an increase in the flux of melt migration between the two magma bodies. The best-fitting double-couple focal mechanisms of the largest swarm events and the dip of the cluster indicate

that this melt influx resulted in primarily sinistral strike-slip faulting on a N-S oriented fault with NW-SE oriented P-axes and NE-SW oriented T-axes, implying sliding in the host rock. The presence of non–double-couple components in these focal mechanisms (Figure S7) suggests an influence of magmatic processes on the faulting. The source process of these events can be explained by brittle failure in the host rocks through dike propagation or dike inflation due to magma ascent (Ukawa & Tsukahara, 1996; Roman, 2005; Roman & Cashman, 2006). As further support for the melt flux increase interpretation, we compare the timing of the observed deep swarm with the vertical displacement data from GPS station MAU2 from Le Mével et al. (2021) where high rates of inflation-related surface uplift have been recorded for several years. This comparison shows that the deep earthquake swarm precedes a marked increase in the inflation-related surface uplift rate by approximately three months (Figure 4a, 4b). Assuming that the increase in melt flux between the magma reservoirs directly led to the increase in uplift rate and using a vertical propagation distance of ~13 km over 3 months, we calculate an approximate hydraulic diffusivity of the upper crustal magma reservoir of ~20 m^2/s following Shapiro et al., (2017), consistent within the experimental range of fractured igneous rocks (Roeloffs, 1996). Similar analysis in other volcanic arc regions have estimated hydraulic diffusivities ranging from 10^{-1} to 10^2 m^2/s (Rothert et al., 2003; Saar & Manga, 2004; Shapiro et al., 2017). This is an approximation using simple assumptions of the fluid pathways within the upper crust plumbing network. It is likely to be more complex, likely with several sub-chambers and storage zones (Cáceres Acevedo, 2016; Cordell et al., 2018). Within silicic melts, diffusivity is also highly dependent on the temperature and its composition (Zhang & Gan, 2022), which we expect to change along the plumbing pathways, and as the melt chemically differentiates. Since the higher inflation rate has sustained at least until 2020, in this context, the deep VT swarm may also represent the establishment of a new pathway for magma ascent and increased connectivity between the deep and shallow magma reservoirs.

The results of this study demonstrate that detection of transcrustal magmatic processes is critical for monitoring volcanic unrest at LdM and potentially other volcanoes around the world. This highlights the need to better understand processes occurring within the mid to lower crust with respect to how they impact surface observations in volcanic regions. Paramount to understanding these deep crustal processes is the detection of DLP and VT earthquakes that may indicate the episodic migration of magma within transcrustal systems and provide critical information for global volcano monitoring networks and local observations at Laguna del Maule.

5.0 Methods

We use the seismic data from the TANGO node and broadband seismometer arrays (network codes XM & 1X; Beck et al., 2022a, 2022b) and LaMa (network code ZR; Thurber, 2015) network for this study. Within the TANGO deployment, a dense linear array of 5 Hz nodal seismometers with average ~2 km spacing was active between January through May 2023. The LaMa network was deployed in stages from January 2015 to April 2018 and surrounded the LdM complex, improving the three-dimensional coverage. We prepare two earthquake catalogs for the LdM volcanic field using the LaMa and TANGO networks within their respective deployment periods using a deep-learning-based earthquake detection workflow (LOC-FLOW: Zhang et al., 2022) and use P-Receiver Functions (RFs; Burdick & Langston, 1977; Langston, 1979) to constrain the local crustal structure. Together, these combined data constrain the crustal structure and trans-crustal deformation occurring beneath LdM.

5.1 Seismicity Analysis

The earthquake catalogs are prepared using the software organized under the LOC-FLOW framework (Zhang et al., 2022) followed by frequency analysis and focal mechanism calculation.

5.1.1 Earthquake detection and Initial Locations:

Seismic P and S phases are picked using a deep neural-network-based phase picker: PhaseNet (Zhu & Beroza, 2018). Several pre-trained deep-learning models stored in Seisbench toolbox (Woollam et al., 2022) are tested on a single day (February 14, 2018) of data with very high seismic activity. The original PhaseNet model (Zhu & Beroza, 2018) and Volpick model (Zhong & Tan, 2024) had the best phase prediction performance (Supplementary Figure S1). However, more events were detected with the original PhaseNet model compared to Volpick (Supplementary Figure S2). Hence, the original PhaseNet model from Zhu and Beroza (2018) is used in this study. A phase prediction with a probability of 0.5 or higher is considered a true seismic phase arrival. These seismic phases are associated with seismic events using a grid search method (REAL; Zhang et al., 2019) where the pick probabilities are used as pick weights. To reduce the false positives, a strict threshold of at least 5 P phases, 5 S phases, 15 total phases, and 5 stations recording both P and S arrivals have been used for the TANGO array. However, due to lesser number of stations and better azimuthal coverage, a weaker threshold of at least 5 P phases, 3 S phases, 10 total phases, and 3 stations recording both P and S arrivals have been used for the LaMa array. The initial hypocenters derived with these constraints are refined with simulated annealing optimization (Kirkpatrick et al., 1983; Zhang et al., 2019).

5.1.2 Earthquake relocation:

The hypocenter locations are refined by jointly updating those with the regional 1D velocity model using the VELEST algorithm (Kissling et al., 1994) starting with the 1D velocity model from Cardona et al. (2018). Events with mean residual error greater than 1 second or azimuthal gap greater than 240° are discarded. The initial and final velocity models and residual histograms for both the datasets are shown in Supplementary Figure S3. Finally, the events are relocated with a double-difference earthquake relocation algorithm (HypoDD; Waldhauser & Ellsworth, 2000) to refine the locations further. Initially, differential travel times are computed from the catalog phase picks, and the algorithm is applied. Then the resulting refined origin time and hypocenters are used to extract differential travel times by waveform cross-correlation. Finally, the inversion is performed jointly using catalog and cross-correlation based differential travel times. The uncertainties associated with these hypocenters are analyzed using a bootstrap resampling method (Waldhauser & Ellsworth, 2000). The resulting mean deviation of latitude, longitude, and depth for each event is considered as the error bound for the event. A few outlier events with unusually high errors are removed from the catalog. The distributions of mean deviations in latitude, longitude, and depth in bootstrap resampling along with the 2σ boundaries is shown in Supplementary Figure S4.

5.1.3 Magnitudes:

Local magnitudes for the earthquakes are estimated from body-wave amplitudes following (Zhang et al., 2022). For each waveform detecting a P or S phase, the original instrument response is removed, and it is convolved with the response function of a Wood-Anderson seismograph. Next, the peak amplitudes are plugged into an empirical relationship (Hutton & Boore, 1987) to calculate local earthquake magnitudes (M_L). For each event, weighted average of the magnitudes from all waveforms are computed using the pick probabilities as weights, and this weighted mean magnitude is reported for each event. The magnitude distributions and estimated b-values for the catalogs are shown in Supplementary Figure S6.

5.1.4 Frequency Index Analysis:

Since seismic events in volcanic setting demonstrate wide range of frequency content in the seismic data, the frequency content of the events is measured with the Frequency Index (FI) metric (Buurman & West, 2010) defined as:

$$FI = \log_{10} \frac{mean(A_{High})}{mean(A_{Low})}$$

Here A_{high} is the amplitude in the high frequency spectral window, and A_{low} is the amplitude in the low-frequency spectral window.

Vertical component waveforms from the stations with available phase picks are used to calculate these mean spectral amplitudes. A 13 second window starting 3 seconds before the picked P-arrival is used after removing the instrument response. A high-pass filter of 1 Hz is applied as well. The high and low spectral bands are selected as 1-5 Hz and 10-20 Hz respectively after visually inspecting several waveforms. To avoid station bias due to path dependent attenuation effect (Buurman & West, 2010), we applied a station correction to each station following Wilding et al. (2023). The median FI measured for all events at each station is subtracted from the FI value of the station. The mean of these corrected FI measurements is assigned as the FI for each event. The resulting FI distribution has a primary mode with a long tail towards low FI (Figure 2) indicating the Long-Period events.

5.1.5 Focal Mechanisms:

Since shallow seismicity has been analyzed in detail in previous studies, we only focus on the deep crustal events obtained in this study. Focal mechanisms are obtained for 4 well-recorded VT swarm events using P-wave first motion polarities. Due to the emergent nature of the polarities for the LP events, we could not obtain focal mechanisms for these events with this polarity-based method. For the VT events, the P-wave first motion polarities are manually picked for each event. The azimuth and take-off angle of the rays travelling from the source to the station are computed with the TauP program (Crotwell et al., 1999) based on the 1D velocity model obtained from the hypocenter relocation step. The focal mechanisms are calculated using MTfit algorithm (Pugh & White, 2018), which takes a Bayesian approach to find the best-fitting moment tensor for the polarity observations through Monte Carlo sampling. Further, 200 samples of azimuths and take-off angles are computed for each polarity observation by incorporating final hypocenter location errors and 10% added noise to the velocity model. These are included in the inversion to account for uncertainties associated with hypocenters and velocity models. The moment tensor with the highest probability value is selected as the focal mechanism solution. The best-fitting double couple mechanisms are shown in Figure 2, and corresponding strike, dip, and rake are listed in Table S1. The results from the focal mechanism analysis are shown in Supplementary Figure S7.

5.2 Receiver Function Analysis

Receiver Functions (RFs) are time-domain waveforms calculated from the deconvolution of radial and vertical components of the 3-component teleseismic seismogram (Burdick & Langston, 1977; Langston, 1979) (Supplementary Figure

S8). The deconvolution of the vertical component from the radial component isolates the P-to-S conversions (Ps) corresponding to discontinuities in seismic impedance (velocity * density) beneath the seismic station. The converted Ps phase has greater slowness than the direct P-wave and arrives at the receiver with a time delay (t_{ps}) which can be used as a depth-proxy assuming a seismic velocity model. Examples of strong impedance discontinuities may include the crustal Moho, orogenic detachments, and the top or bottom of partial melt bodies. The Ps conversion amplitude and polarity indicate a relative decrease (negative, colored blue in figures) or increase (positive, colored red) in down-going seismic velocity. We calculate RFs using a Gaussian filter with a low pass cutoff frequency of 3.7 HZ (Supplementary Figure S9). The frequency of the RF Ps pulse corresponds to the sharpness of the discontinuity with a higher frequency Ps conversion corresponding to a sharper discontinuity (Supplementary Figure S10).

5.2.1 Common Conversion Point (CCP) Stacking

Receiver Functions passing quality control measures (see Supplemental Text A1) were migrated to depth using the Common Conversion Point method (CCP, Deuker & Sheehan, 1997) using the output 1D velocity model from hypocenter relocations on the LaMa network so that seismicity and RF data were consistent and processes with the same velocity model. A modification was made to the 1D input LaMa model so that the velocities consistent with continental crust continue to 55 km depth. Additional CCP images using different seismic velocity models are shown in Supplementary Figure S11 for comparison. The assumed velocity makes little difference in our overall interpretation, but the depth of the discontinuities can change by a few kilometers depending on the velocity model (Supplemental Figure S11).

CCP stacking involves tracing RF-rays back to their piercing points at different latitude-longitude-depth coordinates using the 1D velocity profile under each station and event back-azimuth. Binning centers are spaced every 3 km laterally and 0.5 km in depth. The bins collect all piercing points within 12 km of the bin center, from which the RF amplitudes are averaged using a distance-weighted bootstrap resampling (Eagar et al., 2011). Closer piercing points are given higher resampling probabilities using a spatial normal distribution, with a standard deviation of 4 km. For each bin, we record the bootstrapped average amplitude, amplitude standard deviation, and piercing point hit counts (Supplementary Figure S12).

5.2.2 Multiples Interference

We assume the strong amplitude Ps conversions as primary conversions from associated discontinuities that relate to real crustal structures. However, the impact

of multiples (P and S waves that bounce between a discontinuity and the surface and hence, arrive later) in the P-wave coda may result in interference with deeper primary Ps-conversions. Multiples are usually of lower amplitude compared to their primary conversions but can retain sufficient amplitude if the scattering discontinuity contrast is strong and close to the surface (Sadler & Pulliam, 2023). Within the 50 km crust, the D1 discontinuity is expected to be the only discontinuity that produces multiples that might arrive at the same time and hence, interfere with deeper crustal Ps conversions. The ray path relationships between multiples and velocities can be determined from Zhu and Kanamori (2000) and Zandt et al. (1995). Using the migration velocity model, and assuming a horizontal D1 interface, we observe a potential multiple in the west-east profile (Figure 3c) from the western end of the D1 discontinuity that is produces a negative amplitude at ~36 km depth between D3 and D4. This observation does not change the overall observation of a deep lower crust LVZ marked at the top by D3 that continues to the Moho.

Acknowledgements

This research was funded by the National Science Foundation, award number: EAR-2020935, EAR-2020627, EAR-2027496, and EAR-2021040; and by the National Agency for Research and Development in Chile award number: ANID AFB230001. Figures within this article were developed using General Mapping Tools (GMT 6; Wesel et al., 2019) and PyGMT (Tian et al., 2024), with background topography provided by the Shuttle Radar Topography Mission data (SRTM; Farr et al., 2007). We would like to extend a special acknowledgement towards the many universities and students who had participated in collecting the data used from the TANGO deployments between 2022 and 2024. We especially acknowledge Sergio León-Ríos, Valentina Reyes-Wagner and Diane Comte from the Universidad de Chile; Lía Orosco Segura from the Universidad Católica de Salta; and Steve Roecker from Rensselaer Polytechnic Institute for their contributions in data collection. We also would like to thank Hélène Le Mével from the Carnegie Institute for Science for sharing the processed GPS data to reproduce the GPS displacement time-series plots from Le Mével et al. (2021).

References

Annen, C., Blundy, J. D., & Sparks, R. S. J. (2005). The Genesis of Intermediate and Silicic Magmas in Deep Crustal Hot Zones. *Journal of Petrology*, *47*(3), 505-539. https://doi.org/10.1093/petrology/egi084

Bai, T., Thurber, C., Lanza, F., Singer, B. S., Bennington, N., Keranen, K., & Cardona, C. (2020). Teleseismic Tomography of the Laguna del Maule Volcanic Field in Chile. *Journal of Geophysical Research: Solid Earth*, *125*(8), e2020JB019449. https://doi.org/https://doi.org/10.1029/2020JB019449

Beck, S., Porter, R., Roecker, S., & Kiser, E. (2022a). *TANGO, Collaborative Research: TransANdean Great Orogeny, Broadbands/Argentina deployment* (EarthScope Data Center (IRISDMC). https://www.fdsn.org/networks/detail/XM_2022/

Beck, S., Porter, R., Roecker, S., & Kiser, E. (2022b). *TANGO, Collaborative Research: TransANdean Great Orogeny, Nodes/Chile deployment* (EarthScope Data Center (IRISDMC). https://www.fdsn.org/networks/detail/XN_2022/

Burdick, L. J., & Langston, C. A. (1977). Modeling crustal structure through the use of converted phases in teleseismic body-wave forms. *Bulletin of the Seismological Society of America*, *67*(3), 677-691. https://doi.org/10.1785/BSSA0670030677

Buurman, H., & West, M. E. (2010). *Seismic precursors to volcanic explosions during the 2006 eruption of Augustine Volcano: Chapter 2 in The 2006 eruption of Augustine Volcano, Alaska* [Report](17692). (Professional Paper, Issue. U. S. G. Survey. https://pubs.usgs.gov/publication/pp17692

Cáceres Acevedo, F. A. (2016). Magma storage conditions and eruptive dynamics of post-glacial effusive volcanism at Laguna del Maule Volcanic field. https://repositorio.uchile.cl/handle/2250/140208

Cáceres, F., Castruccio, Á., & Parada, M. A. (2018). Morphology, Effusion Rates, and Petrology of Postglacial Lavas of Laguna del Maule Volcanic Field, Chilean Andes, and Implications for Their Plumbing System. *Geochemistry, Geophysics, Geosystems*, *19*(12), 4925-4944. https://doi.org/https://doi.org/10.1029/2018GC007817

Cardona, C., Tassara, A., Gil-Cruz, F., Lara, L., Morales, S., Kohler, P., & Franco, L. (2018). Crustal seismicity associated to rpid surface uplift at Laguna del Maule Volcanic Complex, Southern Volcanic Zone of the Andes. *Journal of Volcanology and Geothermal Research*, *353*, 83-94. https://doi.org/https://doi.org/10.1016/j.jvolgeores.2018.01.009

Cashman, K. V., Sparks, R. S. J., & Blundy, J. D. (2017). Vertically extensive and unstable magmatic systems: A unified view of igneous processes. *Science*, *355*(6331), eaag3055. https://doi.org/doi:10.1126/science.aag3055

Cassidy, J. F. (1992). Numerical experiments in broadband receiver function analysis. *Bulletin of the Seismological Society of America*, *82*(3), 1453-1474. https://doi.org/10.1785/bssa0820031453

Cesca, S., Letort, J., Razafindrakoto, H. N. T., Heimann, S., Rivalta, E., Isken, M. P., Nikkhoo, M., Passarelli, L., Petersen, G. M., Cotton, F., & Dahm, T. (2020). Drainage of a deep magma reservoir near Mayotte inferred from seismicity and deformation. *Nature Geoscience*, *13*(1), 87-93. https://doi.org/10.1038/s41561-019-0505-5

Chouet, B. A. (1996). Long-period volcano seismicity: its source and use in eruption forecasting. *Nature*, *380*(6572), 309-316. https://doi.org/10.1038/380309a0

Cordell, D., Unsworth, M. J., & Díaz, D. (2018). Imaging the Laguna del Maule Volcanic Field, central Chile using magnetotellurics: Evidence for crustal melt

regions laterally-offset from surface vents and lava flows. *Earth and Planetary Science Letters*, *488*, 168-180. https://doi.org/https://doi.org/10.1016/j.epsl.2018.01.007

Crotwell, H. P., Owens, T. J., & Ritsema, J. (1999). The TauP Toolkit: Flexible Seismic Travel-time and Ray-path Utilities. *Seismological Research Letters*, *70*(2), 154-160. https://doi.org/10.1785/gssrl.70.2.154

Deuker, K. G., & Sheehan, A. F. (1997). Mantle discontinuity structure from midpoint stacks of coverted P to S waves across the Yellowstone hotspot track. *Journal of Geophysical Research*, *102*, 8313-8327. https://doi.org/10.1029/96JB03857

Doocy, S., Daniels, A., Dooling, S., & Gorokhovich, Y. (2013). The human impact of volcanoes: a historical review of events 1900-2009 and systematic literature review. *PLoS Curr*, *5*. https://doi.org/10.1371/currents.dis.841859091a706efebf8a30f4ed7a1901

Drake, R. E. (1976). Chronology of Cenozoic igneous and tectonic events in the central Chilean Andes—Latitudes 35° 30′ to 36° S. *Journal of Volcanology and Geothermal Research*, *1*(3), 265-284. https://doi.org/10.1016/0377-0273(76)90011-1

Dufek, J., & Bergantz, G. W. (2005). Lower Crustal Magma Genesis and Preservation: a Stochastic Framework for the Evaluation of Basalt–Crust Interaction. *Journal of Petrology*, *46*(11), 2167-2195. https://doi.org/10.1093/petrology/egi049

Eagar, K. C., Fouch, M. J., James, D. E., & Carlson, R. W. (2011). Crustal structure beneath the High Lava Plains of eastern Oregon and surrounding regions from receiver function analysis. *Journal of Geophysical Research: Solid Earth*, *116*(B2). https://doi.org/https://doi.org/10.1029/2010JB007795

Farner, M. J., & Lee, C.-T. A. (2017). Effects of crustal thickness on magmatic differentiation in subduction zone volcanism: A global study. *Earth and Planetary Science Letters*, *470*, 96-107. https://doi.org/https://doi.org/10.1016/j.epsl.2017.04.025

Farr, T. G., Rosen, P. A., Caro, E., Crippen, R., Duren, R., Hensley, S., Kobrick, M., Paller, M., Rodriguez, E., Roth, L., Seal, D., Shaffer, S., Shimada, J., Umland, J., Werner, M., Oskin, M., Burbank, D., & Alsdorf, D. (2007). The Shuttle Radar Topography Mission. *Reviews of Geophysics*, *45*(2). https://doi.org/https://doi.org/10.1029/2005RG000183

Feigl, K. L., Le Mével, H., Tabrez Ali, S., Córdova, L., Andersen, N. L., DeMets, C., & Singer, B. S. (2014). Rapid uplift in Laguna del Maule volcanic field of the Andean Southern Volcanic zone (Chile) 2007–2012. *Geophysical Journal International*, *196*(2), 885-901. https://doi.org/10.1093/gji/ggt438

Glazner, A. F., Bartley, J. M., Coleman, D. S., Gray, W., & Taylor, R. Z. (2004). Are plutons assembled over millions of years by amalgamation from small magma chambers? *GSA today*, *14*(5-Apr), 4-11. https://doi.org/10.17615/nspy-zk53

Global Volcanism Program. (2025). *Volcanoes of the World* (Version v. 5.3.1) Smithsonian Institution. https://doi.org/https://doi.org/10.5479/si.GVP.VOTW5-2025.5.3

Grove, T. L., Till, C. B., & Krawczynski, M. J. (2012). The role of H2O in subduction zone magmatism. *Annual Review of Earth and Planetary Sciences*, *40*(1), 413-439. https://doi.org/10.1146/annurev-earth-042711-105310

Hacker, B. R., Kelemen, P. B., & Behn, M. D. (2015). Continental Lower Crust. *Annual Review of Earth and Planetary Sciences*, *43*(Volume 43, 2015), 167-205. https://doi.org/https://doi.org/10.1146/annurev-earth-050212-124117

Hildreth, W., & Fierstein, J. (2024). Two-million-year eruptive history of Laguna del Maule volcanic field. *Journal of South American Earth Sciences*, *148*, 105132. https://doi.org/https://doi.org/10.1016/j.jsames.2024.105132

Hildreth, W., Godoy, E., Fierstein, J., & Singer, B. (2009). Laguna del Maule Volcanic Field: Eruptive History of a Quaternary basalt-to-rhyolite distributed volcanic field on the Andean rangecrest in central Chile. *USGS Report*, 1-145. https://pubs.usgs.gov/publication/70041338

Hildreth, W., & Moorbath, S. (1988). Crustal contributions to arc magmatism in the Andes of Central Chile. *Contributions to Mineralogy and Petrology*, *98*(4), 455-489. https://doi.org/10.1007/BF00372365

Huang, H.-H., Lin, F.-C., Schmandt, B., Farrell, J., Smith, R. B., & Tsai, V. C. (2015). The Yellowstone magmatic system from the mantle plume to the upper crust. *Science*, *348*(6236), 773-776. https://doi.org/doi:10.1126/science.aaa5648

Hutton, L. K., & Boore, D. M. (1987). The ML scale in Southern California. *Bulletin of the Seismological Society of America*, *77*(6), 2074-2094. https://doi.org/10.1785/bssa0770062074

Jaxybulatov, K., Shapiro, N. M., Koulakov, I., Mordret, A., Landès, M., & Sens-Schönfelder, C. (2014). A large magmatic sill complex beneath the Toba caldera. *Science*, *346*(6209), 617-619. https://doi.org/doi:10.1126/science.1258582

Kirkpatrick, S., Gelatt, C. D., & Vecchi, M. P. (1983). Optimization by Simulated Annealing. *Science*, *220*(4598), 671-680. https://doi.org/doi:10.1126/science.220.4598.671

Kissling, E., Ellsworth, W. L., Eberhart-Phillips, D., & Kradolfer, U. (1994). Initial reference models in local earthquake tomography. *Journal of Geophysical Research: Solid Earth*, *99*(B10), 19635-19646. https://doi.org/https://doi.org/10.1029/93JB03138

Klug, J. D., Singer, B. S., Kita, N. T., & Spicuzza, M. J. (2020). Storage and Evolution of Laguna del Maule Rhyolites: Insight From Volatile and Trace Element Contents in Melt Inclusions. *Journal of Geophysical Research: Solid Earth*, *125*(8), e2020JB019475. https://doi.org/https://doi.org/10.1029/2020JB019475

Konstantinou, K. I. (2024). A Review of the Source Characteristics and Physical Mechanisms of Very Long Period (VLP) Seismic Signals at Active Volcanoes. *Surveys in Geophysics*, *45*(1), 117-149. https://doi.org/10.1007/s10712-023-09800-0

Langston, C. A. (1979). Structure under Mount Rainier, Washington, inferred from teleseismic body waves. *Journal of Geophysical Research: Solid Earth*, *84*(B9), 4749-4762. https://doi.org/https://doi.org/10.1029/JB084iB09p04749

Le Mével, H., Córdova, L., Cardona, C., & Feigl, K. L. (2021). Unrest at the Laguna del Maule volcanic field 2005–2020: renewed acceleration of deformation. *Bulletin of Volcanology*, *83*(6), 39. https://doi.org/10.1007/s00445-021-01457-0

Le Mével, H., Feigl, K. L., Córdova, L., DeMets, C., & Lundgren, P. (2015). Evolution of unrest at Laguna del Maule volcanic field (Chile) from InSAR and GPS measurements, 2003 to 2014. *Geophysical Research Letters*, *42*(16), 6590-6598. https://doi.org/https://doi.org/10.1002/2015GL064665

Levin, V., VanTongeren, J. A., & Servali, A. (2016). How sharp is the sharp Archean Moho? Example from eastern Superior Province. *Geophysical Research Letters*, *43*(5), 1928-1933. https://doi.org/https://doi.org/10.1002/2016GL067729

Miller, C. A., Williams-Jones, G., Fournier, D., & Witter, J. (2017). 3D gravity inversion and thermodynamic modelling reveal properties of shallow silicic magma reservoir beneath Laguna del Maule, Chile. *Earth and Planetary Science Letters*, *459*, 14-27. https://doi.org/https://doi.org/10.1016/j.epsl.2016.11.007

Nichols, M. L., Malone, S. D., Moran, S. C., Thelen, W. A., & Vidale, J. E. (2011). Deep long-period earthquakes beneath Washington and Oregon volcanoes. *Journal of Volcanology and Geothermal Research*, *200*(3), 116-128. https://doi.org/https://doi.org/10.1016/j.jvolgeores.2010.12.005

Peterson, D. E., Garibaldi, N., Keranen, K., Tikoff, B., Miller, C., Lara, L. E., Tassara, A., Thurber, C., & Lanza, F. (2020). Active Normal Faulting, Diking, and Doming Above the Rapidly Inflating Laguna del Maule Volcanic Field, Chile, Imaged With CHIRP, Magnetic, and Focal Mechanism Data. *Journal of Geophysical Research: Solid Earth*, *125*(8), e2019JB019329. https://doi.org/https://doi.org/10.1029/2019JB019329

Pugh, D. J., & White, R. S. (2018). MTfit: A Bayesian Approach to Seismic Moment Tensor Inversion. *Seismological Research Letters*, *89*(4), 1507-1513. https://doi.org/10.1785/0220170273

Roeloffs, E. (1996). Poroelastic Techniques in the Study of Earthquake-Related Hydrologic Phenomena. In R. Dmowska & B. Saltzman (Eds.), *Advances in Geophysics* (Vol. 37, pp. 135-195). Elsevier. https://doi.org/https://doi.org/10.1016/S0065-2687(08)60270-8

Rojas, A., Sruoga, P., Lamberti, M. C., Agusto, M., Tondreau, J., Mendoza, N., Daniele, L., & Morata, D. (2022). Unravelling the hydrothermal system of Laguna del Maule restless volcanic field, in the Andean Southern Volcanic Zone (36° 10'S). *Journal of Volcanology and Geothermal Research*, *424*, 107498. https://doi.org/https://doi.org/10.1016/j.jvolgeores.2022.107498

Roman, D. C. (2005). Numerical models of volcanotectonic earthquake triggering on non-ideally oriented faults. *Geophysical Research Letters*, *32*(2). https://doi.org/https://doi.org/10.1029/2004GL021549

Roman, D. C., & Cashman, K. V. (2006). The origin of volcano-tectonic earthquake swarms. *Geology*, *34*(6), 457-460. https://doi.org/10.1130/g22269.1

Rondenay, S. (2009). Upper Mantle Imaging with Array Recordings of Converted and Scattered Teleseismic Waves. *Surveys in Geophysics*, *30*(4), 377-405. https://doi.org/10.1007/s10712-009-9071-5

Rothert, E., Shapiro, S. A., Buske, S., & Bohnhoff, M. (2003). Mutual relationship between microseismicity and seismic reflectivity: Case study at the German Continental Deep Drilling Site (KTB). *Geophysical Research Letters*, *30*(17). https://doi.org/https://doi.org/10.1029/2003GL017848

Rudnick, R. L., & Fountain, D. M. (1995). Nature and composition of the continental crust: A lower crustal perspective. *Reviews of Geophysics*, *33*(3), 267-309. https://doi.org/https://doi.org/10.1029/95RG01302

Rychert, C. A., Rondenay, S., & Fischer, K. M. (2007). P-to-S and S-to-P imaging of a sharp lithosphere-asthenosphere boundary beneath eastern North America. *Journal of Geophysical Research: Solid Earth*, *112*(B8). https://doi.org/https://doi.org/10.1029/2006JB004619

Saar, M. O., & Manga, M. (2004). Depth dependence of permeability in the Oregon Cascades inferred from hydrogeologic, thermal, seismic, and magmatic modeling constraints. *Journal of Geophysical Research: Solid Earth*, *109*(B4). https://doi.org/https://doi.org/10.1029/2003JB002855

Sadler, B., & Pulliam, J. (2023). Modeling Crustal Structure in the Permian Basin by Waveform-Matching P Receiver Functions and Autocorrelograms With Particle Swarm Optimization. *Journal of Geophysical Research: Solid Earth*, *128*(6), e2023JB026730. https://doi.org/https://doi.org/10.1029/2023JB026730

Shapiro, N. M., Droznin, D. V., Droznina, S. Y., Senyukov, S. L., Gusev, A. A., & Gordeev, E. I. (2017). Deep and shallow long-period volcanic seismicity linked by fluid-pressure transfer. *Nature Geoscience*, *10*(6), 442-445. https://doi.org/10.1038/ngeo2952

Song, Z., Tan, Y. J., & Roman, D. C. (2023). Deep Long-Period Earthquakes at Akutan Volcano From 2005 to 2017 Better Track Magma Influxes Compared to Volcano-Tectonic Earthquakes. *Geophysical Research Letters*, *50*(10), e2022GL101987. https://doi.org/https://doi.org/10.1029/2022GL101987

Thurber, C. (2015). *Laguna del Maule Seismic Imaging* (https://doi.org/10.7914/SN/ZR_2015

Tian, D., Uieda, L., Leong, W. J., Fröhlich, Y., Schlitzer, W., Grund, M., Jones, M., Toney, L., Yao, J., Tong, J.-H., Magen, Y., Materna, K., Belem, A., Newton, T., Anant, A., Ziebarth, M., Quinn, J., & Wessel, P. (2024). PyGMT: A Python interface for the Generic Mapping Tools - v0.14.0. In.

Ukawa, M., & Tsukahara, H. (1996). Earthquake swarms and dike intrusions off the east coast of Izu Peninsula, central Japan. *Tectonophysics*, *253*(3), 285-303. https://doi.org/https://doi.org/10.1016/0040-1951(95)00077-1

Ulmer, P. (2001). Partial melting in the mantle wedge — the role of H2O in the genesis of mantle-derived 'arc-related' magmas. *Physics of the Earth and Planetary Interiors*, *127*(1), 215-232. https://doi.org/https://doi.org/10.1016/S0031-9201(01)00229-1

Vigide, N., Olivar, J., Mescua, J., Basualto, D., Farías, C., Tassara, A., & García, S. (2025). A transpressive stress regime for the Laguna del Maule Volcanic Complex. *Journal of South American Earth Sciences*, *161*, 105563. https://doi.org/https://doi.org/10.1016/j.jsames.2025.105563

Waldhauser, F., & Ellsworth, W. L. (2000). A Double-Difference Earthquake Location Algorithm: Method and Application to the Northern Hayward Fault, California. *Bulletin of the Seismological Society of America*, *90*(6), 1353-1368. https://doi.org/10.1785/0120000006

Wech, A. G., Thelen, W. A., & Thomas, A. M. (2020). Deep long-period earthquakes generated by second boiling beneath Mauna Kea volcano. *Science*, *368*(6492), 775-779. https://doi.org/doi:10.1126/science.aba4798

Wespestad, C. E., Thurber, C. H., Andersen, N. L., Singer, B. S., Cardona, C., Zeng, X., Bennington, N. L., Keranen, K., Peterson, D. E., Cordell, D., Unsworth, M., Miller, C., & Williams-Jones, G. (2019). Magma Reservoir Below Laguna del Maule Volcanic Field, Chile, Imaged With Surface-Wave Tomography. *Journal of Geophysical Research: Solid Earth*, *124*(3), 2858-2872. https://doi.org/https://doi.org/10.1029/2018JB016485

Wessel, P., Luis, J. F., Uieda, L., Scharroo, R., Wobbe, F., Smith, W. H. F., & Tian, D. (2019). The Generic Mapping Tools Version 6. *Geochemistry, Geophysics, Geosystems*, *20*(11), 5556-5564. https://doi.org/https://doi.org/10.1029/2019GC008515

White, R. A., Newhall, C., & Punongbayan, R. (1996). Precursory deep long-period earthquakes at Mount Pinatubo: Spatio-temporal link to a basalt trigger. *Fire and mud: Eruptions and lahars of Mount Pinatubo, Philippines*, 307-328. https://pubs.usgs.gov/pinatubo/white/

Wilding, J. D., Zhu, W., Ross, Z. E., & Jackson, J. M. (2023). The magmatic web beneath Hawai'i. *Science*, *379*(6631), 462-468. https://doi.org/doi:10.1126/science.ade5755

Woollam, J., Münchmeyer, J., Tilmann, F., Rietbrock, A., Lange, D., Bornstein, T., Diehl, T., Giunchi, C., Haslinger, F., Jozinović, D., Michelini, A., Saul, J., & Soto, H. (2022). SeisBench—A Toolbox for Machine Learning in Seismology. *Seismological Research Letters*, *93*(3), 1695-1709. https://doi.org/10.1785/0220210324

Zandt, G., Myers, S. C., & Wallace, T. C. (1995). Crust and mantle structure across the Basin and Range-Colorado Plateau boundary at 37°N latitude and implications for Cenozoic extensional mechanism. *Journal of Geophysical Research: Solid Earth*, *100*(B6), 10529-10548. https://doi.org/https://doi.org/10.1029/94JB03063

Zhang, M., Ellsworth, W. L., & Beroza, G. C. (2019). Rapid Earthquake Association and Location. *Seismological Research Letters*, *90*(6), 2276-2284. https://doi.org/10.1785/0220190052

Zhang, M., Liu, M., Feng, T., Wang, R., & Zhu, W. (2022). LOC-FLOW: An End-to-End Machine Learning-Based High-Precision Earthquake Location Workflow. *Seismological Research Letters*, *93*(5), 2426-2438. https://doi.org/10.1785/0220220019

Zhang, Y., & Gan, T. (2022). Diffusion in Melts and Magmas. *Reviews in Mineralogy and Geochemistry*, *87*(1), 283-337. https://doi.org/10.2138/rmg.2022.87.07

Zhong, Y., & Tan, Y. J. (2024). Deep-Learning-Based Phase Picking for Volcano-Tectonic and Long-Period Earthquakes. *Geophysical Research Letters*, *51*. https://doi.org/10.1029/2024GL108438

Zhu, L., & Kanamori, H. (2000). Moho depth variation in southern California from teleseismic RFs. *Journal of Geophysical Research*, *105*, 2969-2980. https://doi.org/10.1029/1999JB900322

Zhu, W., & Beroza, G. C. (2018). PhaseNet: a deep-neural-network-based seismic arrival-time picking method. *Geophysical Journal International*, *216*(1), 261-273. https://doi.org/10.1093/gji/ggy423

Supplementary Files

This is a list of supplementary files associated with this preprint. Click to download.

- LagunaDeLMauleSupplementaryMaterial.pdf